Infrared Physics & Technology 133 (2023) 104865

Contents lists available at ScienceDirect

Infrared Physics and Technology

journal homepage: www.elsevier.com/locate/infrared

Laser photo-acoustic methane sensor (7.7 μm) for use at unmanned aerial vehicles

I.V. Sherstov [a,b,c,*], D.B. Kolker [a,b,c,†], V.A. Vasiliev [a], A.V. Pavlyuk [b], M.B. Miroshnichenko [b], A.A. Boyko [a,b], N.Yu. Kostyukova [a,b,c], I.B. Miroshnichenko [a,c]

[a] Institute of Laser Physics SB RAS, 15B, Ac. Lavrentieva Ave., Novosibirsk 630090, Russia
[b] Novosibirsk State University, 1, Pirogova St., Novosibirsk 630090, Russia
[c] Novosibirsk State Technical University, 20, Karl Marx Ave., Novosibirsk 630073, Russia

ARTICLE INFO

Keywords:
Methane
Photo-acoustic gas analyzer
Quantum-cascade laser
Resonant differential photo-acoustic detector
UAV

ABSTRACT

A compact laser photo-acoustic (PA) methane sensor based on a quantum-cascade laser (~7.7 μm; 1750 Hz; 25 mW), a resonant differential photo-acoustic detector (PAD), and a sealed-off gas-filled PA *Ref*-cell has been developed. Normalization of the absorption signals in the PAD is carried out according to the absorption signals in the gas-filled PA *Ref*-cell, which significantly reduces the measurement errors of the methane concentration in the case of instability of the laser emission wavelength. The minimum measured background signal of the PA sensor (using high purity nitrogen) is $n_{min} \approx (26.6 \pm 8.4)$ ppb CH_4 (at a bandwidth of 20 Hz), the value of normalized noise equivalent absorption ($NNEA$) = 8.22×10^{-10} $cm^{-1} \cdot W/Hz^{1/2}$. A comparison of various research groups results with mid-IR PA gas analyzers is carried out. The developed PA methane sensor is adapted for placement on the UAV's board. Device has dimensions of 315 × 165 × 110 mm, weight ~3.1 kg, power supply from an external source (9…60 VDC), power consumption ~20 VA.

1. Introduction

Currently, various methods of remote sensing of the Earth using unmanned aerial vehicles (UAVs) are widely used during geological and geophysical works. Different indirect methods, such as aeromagnetic survey, gamma spectrometry and others [1], are used to detect potential deposits of oil and natural gas during exploration work. A promising addition to traditional search methods is the direct measurement of the CH_4 concentration in the surface layer of the atmosphere above the surveyed area, since natural gas (~90% methane) seeps through the soil to the Earth's surface under natural pressure. The average CH_4 background concentration in the atmosphere is ~1.9 ppm [2,3]. A marked excess of this average local CH_4 concentration in the air will indicate the location of a potential oil or gas field.

In this regard, the task of building a highly sensitive methane sensor with small dimensions, weight and power consumption, which can be installed on a UAV [4] to measure the background concentration of CH_4 in the air in the surface layer of the atmosphere over vast territories in real time, becomes relevant. The main suitability parameter of such a methane sensor is its threshold sensitivity, which should ensure reliable registration of the average CH_4 background concentration in the air (from ~2 ppm and higher) with a signal-to-noise ratio (SNR) of at least 10…20.

The most sensitive modern methods of gas analysis are gas chromatography (GC) and mass spectrometry (MS), as well as their combination [5,6]. These methods are implemented mainly in laboratory conditions, have unsurpassed sensitivity and selectivity. However, GC and MS gas analyzers cannot operate in real time and in the field conditions, which is often necessary in practice. Note that gas analyzers using laser methods for detecting various gas impurities (for example, the use of multipass cells [7], tunable diode laser spectroscopy (TDLS) [8,9], cavity ring-down spectroscopy (CRDS) [10] and others [11,12]) can operate in real time, in the field conditions, and even remotely (LIDAR systems) [13].

The method of laser photo-acoustic spectroscopy (LPAS) [14] is one of the highly sensitive methods of laser gas analysis of the atmosphere and other gas mixture, which makes it possible to locally measure the microconcentrations of various impurity and pollutant gases in real

* Corresponding author at: Institute of Laser Physics SB RAS, 15B, Ac. Lavrentieva Ave., Novosibirsk 630090, Russia.
E-mail address: sherstov@ngs.ru (I.V. Sherstov).
† Deceased author.

https://doi.org/10.1016/j.infrared.2023.104865
Received 16 June 2023; Received in revised form 4 August 2023; Accepted 12 August 2023
Available online 13 August 2023

time. It is based on the effect of absorption of modulated laser radiation by the investigated gas impurity (marker gas). An important condition for the implementation of the LPAS method is the coincidence of the wavelength of the probing laser radiation and the absorption band of the gas under study. Usually, laser radiation, modulated in amplitude or in frequency of emission, passes through a photo-acoustic detector (PAD) filled with a gas mixture with an admixture of the studied marker gas. As a result of the absorption of the modulated probing radiation by the marker gas molecules due to the photo-acoustic effect, pressure oscillations are formed in the PAD, which are recorded by a microphone located on the PAD's wall. There are other schemes for measuring PA signals using quartz tuning forks (QEPAS technology) [15] and cantilevers (CEPAS technology) [16].

Methane has two strong absorption bands located in the mid-IR spectral regions near ~3.3 μm and ~7.7 μm [17,18], as well as a weak absorption band near ~1.65 μm (band overtone absorption at ~3.3 μm). Various research groups in the world use all three absorption bands of methane to build the laser gas analyzers of CH_4 [19–31], including for placement on UAVs and aircrafts [32–42]. In our experimental works [30,31], both strong CH_4 absorption bands (~3.3 and ~7.7 μm) were used to detect methane impurities in the air.

This work is a continuation of our studies of the CH_4 laser PA gas analyzer [31] based on a quantum-cascade laser (~7.7 μm) and a resonant differential PAD. The purpose of this work is to develop a compact airborne highly sensitive laser PA methane sensor for its installation on the UAV's board in order to detect places with an increased background concentration of CH_4 during search operations in the field conditions.

2. Experimental setup

The studies were carried out on the experimental setup shown in Fig. 1. The main optical elements of the studied PA methane gas analyzer are quantum cascade laser (QCL), resonant differential PAD, sealed-off gas-filled PA *Ref*-cell, and pyrodetector. The absorption signals in the measuring PAD were normalized according to the absorption signals in the sealed-off gas-filled PA *Ref*-cell. Similar scheme for constructing a laser photoacoustic gas analyzer using a gas-filled PA *Ref*-cell for normalizing absorption signals in a resonant PAD was first used in [43], where a sufficiently high accuracy (~5%) of measuring the concentration of the gas under study was noted.

2.1. Radiation source

In this work, we used mid-IR quantum-cascade laser (QD7500CM1 model, Thorlabs), which operates at $\lambda \approx 7.65$ μm with a pulse repetition frequency f_{PRF} (duty cycle 50%) equal to the lowest resonant frequency of the differential PAD ($f_1 \approx 1750…1780$ Hz). The laser was housed in the metal holder with temperature stabilization (own design; unit dimensions 70 × 70 × 38 mm; weight ~450 g). The QCL emission wavelength depends on its operating temperature (see experimental graph in [31]), which is maintained by the laser's thermostat. The QCL current and temperature are managed by a controller (own development).

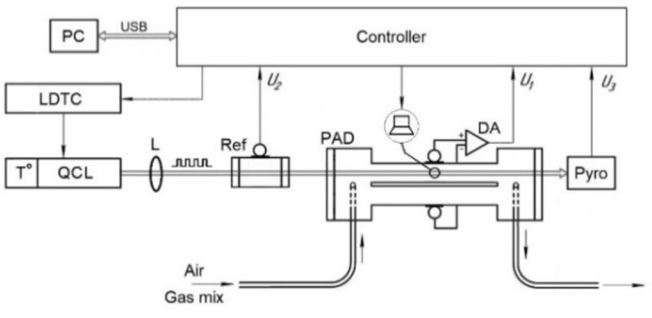

Fig. 1. Scheme of the experimental setup: *QCL* – quantum cascade laser; *T°* – laser's thermostat; *LDTC* – laser current and thermostat controller; *L* – lens; *Ref* – sealed-off gas-filled PA cell; *PAD* – resonant differential photo-acoustic detector; *Pyro* – pyrodetector; *DA* – differential amplifier; *PC* – computer.

A beam of repetitively pulsed QCL's radiation (see Fig. 1) passes successively through a lens, sealed-off gas-filled PA *Ref*-cell, resonant differential PAD, and incidents on pyrodetector (MG-30 model). The QCL emission wavelength is tuned to the maximum of the CH_4 absorption band near $\lambda \approx 7.652$ μm according to the absorption signal in the sealed-off gas-filled PA *Ref*-cell. The pyrodetector was used to adjust the optical scheme of PA gas analyzer and control the QCL radiation power.

Electrical signals from the resonant differential PAD (U_1), the sealed-off gas-filled PA *Ref*-cell (U_2), and the pyrodetector (U_3) are fed to the corresponding ADC inputs of the controller (see Fig. 1), which is connected to the computer. Registration, processing and display of experimental data is carried out on computer using the control program "*ILPA*" (program and electronics was developed by V.A. Vasiliev; ILP SB RAS).

2.2. Block of photo-acoustic detectors

A resonant differential PAD with a small length of buffer cavities (Sherstov's scheme [48]; OAD-90 model) was used as a measuring detector applied in a number of works by various authors [25,27,31,44–53]. The first version of this detector (prototype, 2007) was used in our work [54].

The structure diagram of the resonant differential OAD-90 detector and its appearance are shown in Fig. 2a, b. In 2007–2012, a series of these detectors was manufactured for use as part of a highly sensitive SF_6 laser PA leak detector [46,47,50]. The detectors are made of a hard aluminum alloy and contain two parallel acoustic resonators (Ø9 × 90 mm) separated by a thin partition (thickness 1 mm). The ends of the acoustic resonators exit from both sides into buffer cavities (Ø20 × 8…10 mm), which are closed by flanges with transparent anti-reflective windows (ZnSe; AR 7.7 μm). The walls of acoustic resonators and buffer cavities of the detector are polished.

Note that, in contrast to paper [55] (the original Miklos's scheme), in the resonant differential OAD-90 detector, the length of buffer cavities (8…10 mm) is small and comparable to the diameter of acoustic resonators (Ø9 mm), which has its advantages (see [48]). The gas input/output is carried out through hoses (inner Ø2 mm) installed on the side walls of the buffer cavities symmetrically with respect to the PAD's acoustic resonators. When developing and manufacturing the resonant differential OAD-90 detector, some recommendations from paper [56] were taken into account.

In the middle of each acoustic resonator of the differential OAD-90 detector, there is one electret microphone, matched in pairs with a response imbalance of ~2…3%. The microphones are connected to the inputs of a gain-balanced differential amplifier separately per channel (for precise balancing of microphone responses). In the middle of one of the acoustic resonators of differential OAD-90 detector, opposite the microphone, a small-sized piezoelectric sound emitter (CPE-171 model) is installed, which is used for short-term pulsed excitation of the detector's own acoustic oscillations and determining its lowest resonant frequency (f_1). The measurement of the PAD's lowest resonant frequency is carried out practically in real time (for ~0.1 s) with an error of no more than ±0.1 Hz, as described in our paper [44].

The lowest resonant frequency of resonant differential OAD-90 detector is $f_1 \approx 1750$ Hz (when filled with air) or $f_1^* \approx 1780$ Hz (when filled with nitrogen), the quality factor of the resonances is $Q \approx 54$. As shown in papers [21,48], at the lowest resonant frequency (f_1) of differential OAD-90 detector, an acoustic mode (standing wave) is formed with the ring trajectory of pressure oscillations propagation, covering both acoustic resonators of the detector. At the same time, at the lowest resonant frequency f_1, antinodes of pressure oscillations (in antiphase) are located in the middle of both acoustic resonators of the differential

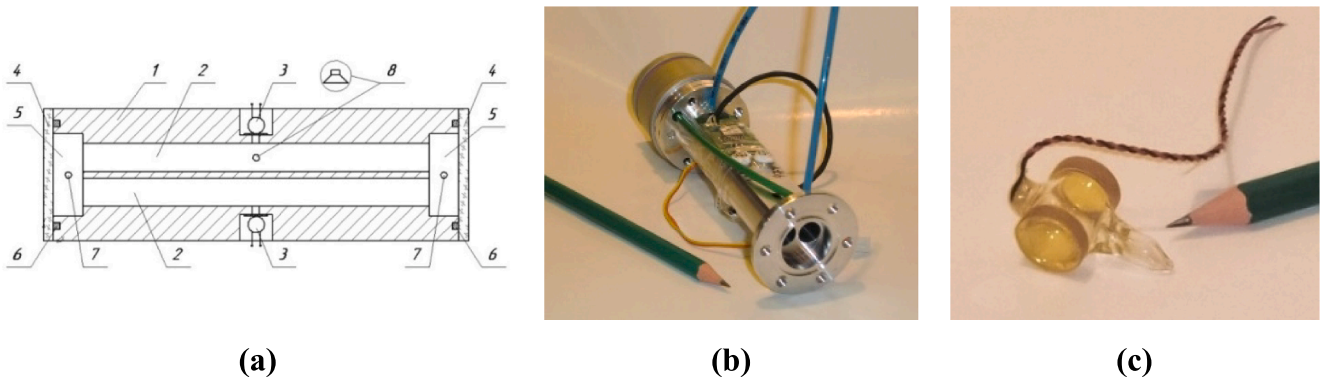

Fig. 2. **(a)** – Scheme of resonant differential PAD with a small length of buffer cavities (Sherstov's scheme): *1* – PAD's body; *2* – acoustic resonators; *3* – microphones; *4* – enlightened windows; *5* – buffer cavities; *6* – rubber seals, *7* – holes for gas input-output; *8* – sound emitter; **(b)** – Photo of the resonant differential OAD-90 detector; **(c)** – Photo of the sealed-off gas-filled PA *Ref*-cell.

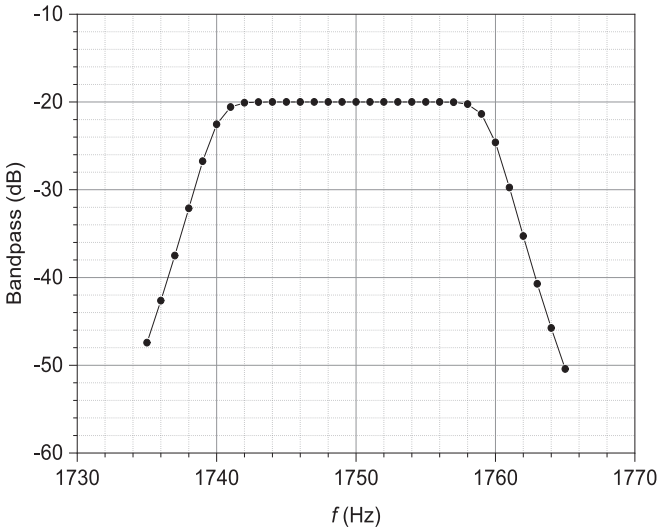

Fig. 3. Bandwidth of the electronic signal registration system.

PAD, and the nodes of pressure oscillations are located in buffer cavities, protruding slightly from the acoustic resonators of the detector by 1…1.5 mm [48]. We note a very important property of the described resonant ring acoustic mode of the differential PAD: the propagation trajectory of pressure oscillations does not reach the detector's windows, which significantly increases the immunity of this differential PAD from the parasitic effect of absorption in the detector's windows.

Looking a little ahead (see Fig. 5a), we can calculate that at average QCL radiation power of $P_0 = 25$ mW ($\lambda = 7.652$ μm) and filling the differential OAD-90 detector with the $N_2 + 9.7$ ppm CH_4 test gas mixture (which corresponds to the absorption parameter $\alpha = 1.7 \times 10^{-4}$ cm^{-1}), the response of the OAD-90 detector at lowest resonant frequency f_1 is $U_1 \approx 115$ μV (with one connected microphone), which corresponds to the detector conversion coefficient $\eta_1 \approx 27$ V/W·cm^{-1}. When two microphones of the differential OAD-90 detector are connected, the conversion coefficient is $\eta_2 \approx 54$ V/W·cm^{-1}.

The sealed-off gas-filled *Ref*-cell is a nonresonant PA cell. It is made in the form of a hermetic glass flask Ø12 × 12 mm in size (see Fig. 2c), to the ends of which the transparent ZnSe windows with AR coating (7.7 μm) are glued. A microphone is glued to the side wall of the cell, connected by a hole to the inner volume of the flask. The cell was filled with a gas mixture of N_2 + 1% CH_4 to atmospheric pressure, after which it

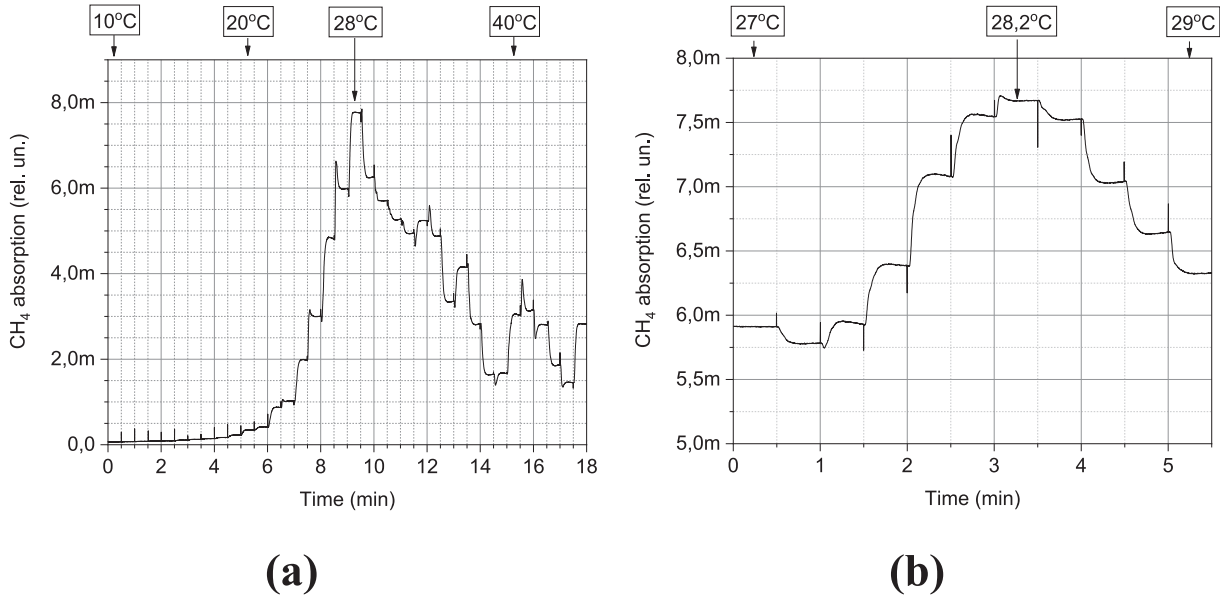

Fig. 4. Methane absorption measurement in a sealed-off gas-filled PA *Ref*-cell (normalized by QCL power) with a stepwise change in QCL temperature: **(a)** – in the range of 10…46 °C, step 1 °C; **(b)** – in the range of 27…29 °C, step 0.2 °C.

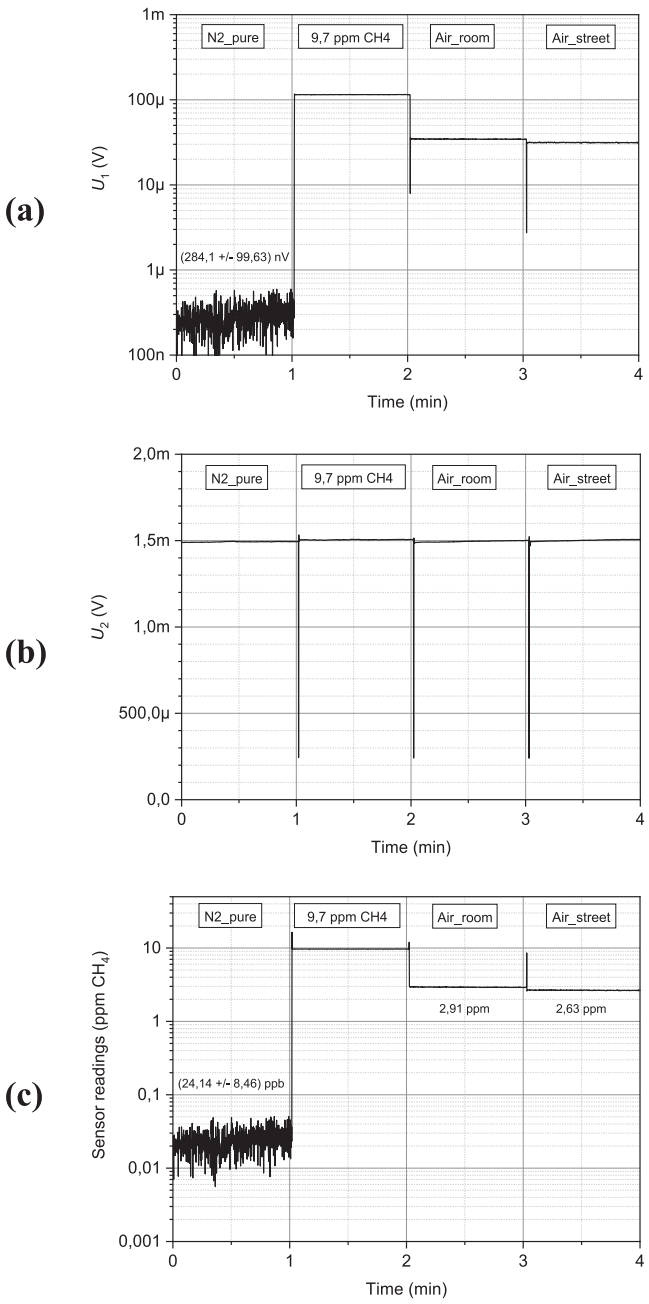

Fig. 5. Experimental recordings of signals of the PA methane sensor when the resonant differential OAD-90 detector was equipped with microphones of HBO1003D-46/1342 model (Ø9.7 mm): **(a)** – response from one of detector's microphones; **(b)** – response from the sealed-off gas-filled PA *Ref*-cell; **(c)** – calibrated readings of the PA methane sensor. The measuring OAD-90 detector was sequentially filled with high-purity nitrogen, a test gas mixture (N_2 + 9.7 ppm CH_4), room air, and street air (fragments lasting 1 min each).

was sealed off. Similar sealed-off gas-filled PA *Ref*-cells were previously successfully used in our works [31,45–47,50].

Note that in the measuring resonant differential OAD-90 detector and the sealed-off gas-filled PA *Ref*-cell, volumetric absorption of probing laser radiation occurs, which does not require the use of lasers with a high beam quality (TEM_{00} mode or similar), as, for example, in the case of QEPAS sensors [15] or other methods.

2.3. Measurement of methane concentration

The essence of the optical scheme of a laser PA gas analyzer using a sealed-off gas-filled PA *Ref*-cell is that, upon random tuning of the laser emission wavelength ($\lambda_i \pm \Delta\lambda$), the absorption cross section of the tracer gas impurity ($\sigma(\lambda_i) \pm \Delta\sigma$) filling the measuring PAD (with concentration n_1) and the PA *Ref*-cell (with concentration n_2) will change synchronously in the PAD and the PA *Ref*-cell. Therefore, when normalizing the absorption signals in the measuring PAD (U_1) by the absorption signals in the gas-filled PA *Ref*-cell (U_2), not only normalization by the laser radiation power (as usual when using a power meter) is possible, but also a significant compensation of the influence of the wavelength instability ($\lambda_i \pm \Delta\lambda$) on the result of measuring the concentration of the gas under study (n_1). In our work [46], we present an analysis of various schemes for constructing the laser PA SF_6 gas analyzer using sealed-off gas-filled PA *Ref*-cells, as well as the results of experimental studies of these optical schemes.

In our case (see Fig. 1), to measure the concentration of CH_4 (n_1) in the analyzed gas sample, the absorption signals in the measuring differential OAD-90 detector (U_1) are normalized according to the absorption signals in the sealed-off gas-filled PA *Ref*-cell (U_2). In this case, the ratio of measured signals (U_1/U_2) can be written as:

$$\frac{U_1}{U_2} = T_w^2 \cdot \frac{S_1(f_1)}{S_2(f_1)} \cdot \left[\frac{1 - e^{-\tau_1}}{1 - e^{-\tau_2}}\right] \cdot e^{-\tau_2} \quad (1)$$

where $\tau_1 = n_1 \cdot \sigma(\lambda_i) \cdot l_1$ and $\tau_2 = n_2 \cdot \sigma(\lambda_i) \cdot l_2$ are the optical thicknesses of the PAD and the gas-filled PA *Ref*-cell, respectively; l_1 and l_2 are the lengths of the PAD and the gas-filled PA *Ref*-cell, respectively; T_w is the transparency of optical windows; $S_1(f_1)$ and $S_2(f_1)$ are the sensitivity (response) of the PAD and the gas-filled PA *Ref*-cell at the resonant frequency f_1, respectively.

In the weak absorption approximation (when $\tau_1, \tau_2 \ll 1$) formula (1) is noticeably simplified:

$$\frac{U_1}{U_2} = T_w^2 \cdot \frac{S_1(f_1)}{S_2(f_1)} \cdot \left[\frac{n_1 \cdot \sigma(\lambda_i) \cdot l_1}{n_2 \cdot \sigma(\lambda_i) \cdot l_2}\right] \cdot e^{-\tau_2} \quad (2)$$

where we can determine the desired value n_1 of studied gas concentration filling the measuring PAD [46]:

$$n_1 = C_{12}(f_1) \cdot \frac{U_1}{U_2} \cdot [1 + \tau_2(\lambda_i)] \quad (3)$$

$$C_{12}(f_1) = \left[\frac{S_2(f_1)}{S_1(f_1)} \cdot \frac{1}{T_w^2} \cdot \frac{n_2 \cdot l_2}{l_1}\right] \quad (4)$$

where the factor $C_{12}(f_1)$ includes terms that depend only on the laser pulse repetition rate.

As can be seen from expression (3), with an uncontrolled change in the wavelength of the laser radiation ($\lambda_i \pm \Delta\lambda$) the main contribution to the measurement errors of the concentration value n_1 can be made by the last factor $[1 + \tau_2(\lambda_i \pm \Delta\lambda)]$. Let us rewrite formula (3) in the form:

$$n_1 = C_{12}(f_1) \cdot \frac{U_1}{U_2} \cdot [1 + \tau_2(\lambda_i) \pm \Delta\tau_2] \quad (5)$$

where $\Delta\tau_2$ is the change in the optical thickness $\tau_2(\lambda_i)$ as the wavelength changes by $\pm\Delta\lambda$. By choosing the design parameters of the sealed-off gas-filled PA *Ref*-cell and laser's operating mode, it is possible to ensure the condition $\Delta\tau_2 \ll [1 + \tau_2(\lambda_i)]$, when variations in $\pm\Delta\tau_2$ during tuning of the emission wavelength ($\lambda_i \pm \Delta\lambda$) will lead to relative variations in the measured value n_1 no more than ±3…5%.

Let us give some examples. Earlier in our paper [46], we described the development of PA SF_6 leak detector based on a waveguide CO_2 laser with RF excitation, a resonant differential PAD and a sealed-off gas-filled PA *Ref*-cell (the optical scheme of the SF_6 leak detector is similar to that in Fig. 1). The CO_2 laser operated in the free running mode with spontaneous

tuning of the wavelength around $\lambda \approx 10.6$ μm (10P(16)…10P(26) emission lines; $\nu \approx 938.69…947.74$ cm^{-1}), where is a strong broad SF_6 absorption band centered at $\nu = 947.9$ cm^{-1} [17,18]. Normalization of the absorption signals in the measuring differential PAD (OAD-90 model) was carried out according to the absorption signals in the gas-filled PA *Ref*-cell. During long-term experimental recordings (20 min), the signals from the microphones of the measuring differential PAD (U_1) and the gas-filled PA *Ref*-cell (U_2), due to the instability of the laser emission wavelength ($\lambda_i \pm \Delta\lambda$) and the change in absorption of the SF_6 impurity ($\sigma(\lambda_i) \pm \Delta\sigma$), experienced large relative variations up to 50%. However, the signal ratio (U_1/U_2) showed low level of relative variation of the measured SF_6 concentration ($n_1 = 40$ ppm) not more than 3…4%.

In our work [31], we studied a bench version of a laser photoacoustic methane sensor, the optical scheme of which corresponds to Fig. 1. When the operating temperature of the QCL was changed in the range of 26…30 °C, the laser emission wavelength changed in the range of ~7651.5…7653.5 nm, passing through the absorption peak of methane (see, for example, Fig. 4). When the CH_4 absorption signals in the measuring differential PAD (U_1) were normalized to the QCL radiation power (using a pyrodetector; U_3), the relative variations in the measured CH_4 concentration ($n_1 = 97$ ppm) due to tuning of the laser emission wavelength reached ~25%. When the CH_4 absorption signals in the measuring differential PAD were normalized by the absorption signals in the sealed-off gas-filled PA *Ref*-cell (U_2), the relative variations in the measured methane concentration under the same conditions did not exceed 3%.

Thus, in our works [31,46] it is experimentally shown that under conditions of instability of the laser emission wavelength ($\lambda_i \pm \Delta\lambda$), the relative error in measuring the concentration n_1 of the studied gas impurity (SF_6, CH_4) when normalizing the absorption signals in the measuring PAD according to the absorption signals in the sealed-off gas-filled PA *Ref*-cell decreases at least 10…15 times compared to the traditional normalization by the laser radiation power.

3. Experimental results

3.1. Brief description of the operation of electronic signal registration system

During the experiments, the signals of the resonant differential OAD-90 detector (U_1), the sealed-off gas-filled PA *Ref*-cell (U_2), the pyrodetector (U_3), as well as the ratio of signals (U_1/U_2) with subsequent calibration of this ratio by the known concentration of methane impurities (n_1) in the test gas mixtures were measured and recorded. When measuring and recording these signals, a multichannel ADC board (24 bits; 4 channels) and the "*ILPA*" control program were used.

The "*ILPA*" program carries out continuous simultaneous data acquisition from all ADC channels. When the buffer in memory is full, the information arrives for further processing. The data is multiplied by a synthesized LO signal in the complex representation (in-phase and quadrature components), whose frequency corresponds to the resonant frequency f_1, after which an 8th order digital Butterworth low-pass filter with a user-defined bandwidth is applied to the data.

Thus, per-channel quadrature demodulation (*I/Q downconvert*) of signals at the fundamental frequency f_1 is carried out. The complex data obtained at this stage contain information about the amplitude and phase of the signals at the operating frequency f_1 in each of the ADC channels. Further, the data of the signal channel (response of resonant differential PAD) is divided into the data of the reference channel (response of gas-filled PA *Ref*-cell or pyrodetector), conversion to the polar form of representation, averaging and decimation.

As a result, from the original data stream with a frequency of 48 kHz, an output signal with a lower sampling rate (10 Hz by default) is generated, proportional to the ratio of signals at the fundamental frequency f_1 in the signal and reference channels.

To calculate the threshold sensitivity of the PA methane sensor being developed (the *NNEA* parameter), it is necessary to determine the bandwidth of the electronic registration system. To do this, a test signal (sine, 1750 Hz, 100 mV) was sent to the input of the ADC board from a sound oscillator. The detection frequency of the recording system was discretely tuned manually by the operator in 1 Hz steps in the range of 1735…1765 Hz. The response of the registration system to the test signal is shown in Fig. 3; the bandwidth is $BP \approx 20$ Hz (at –3 dB level).

3.2. Selecting the laser's operating point

To fine-tune the laser emission wavelength to CH_4 absorption peak near $\lambda \approx 7.65$ μm, the ratio (U_2/U_3) of the signals from the sealed-off gas-filled PA *Ref*-cell (U_2) and the pyrodetector (U_3) was measured during stepwise scanning of the QCL operating temperature in the range of 10…46 °C in steps of 1 °C every 30 s (see Fig. 4a). It was found that the absorption peak of methane is observed at a QCL temperature of about $T_{QCL} = 28$ °C. A similar stepwise scanning of the QCL temperature in the range of 27…29 °C with a step of 0.2 °C (see Fig. 4b) showed that the maximum absorption of methane is observed at the QCL temperature $T_{QCL} = 28.2$ °C, which was entered into the memory of the control program of the PA methane sensor being developed and subsequently used in all experiments.

3.3. Selecting microphones for the resonant differential OAD-90 detector

For a long time (2007–2020), resonant differential OAD-90 detectors used as part of SF_6 laser PA leak detectors [46,47,50] based on a waveguide CO_2 laser with RF pumping (average radiation power ~250 mW) were equipped with inexpensive electret microphones (EM-6050, WM-61, CME-1538 models, etc.), which have SNR ~60 dB (see Table 1, pos. 1–3).

However, when developing PA gas analyzers using other types of radiation sources with a lower average radiation power (for example, OPO [30] or QCL [31]), the intrinsic noise of these microphones began to limit the threshold sensitivity of the developed PA gas analyzers. Therefore, several samples of the resonant differential OAD-90 detector were modified to install and test other types of low-noise electret microphones with a higher SNR ~76…80 dB (see Table 1, pos. 4–8). In the course of finalizing the design of OAD-90 detectors, the landing sockets for installing the new electret microphones (Ø8 mm and Ø9.7 mm) were changed, the rest of the parameters remained unchanged.

3.4. Study of the threshold sensitivity of PA methane sensor

Comparative studies of the threshold sensitivity of PA methane sensor being developed (see Fig. 1) were carried out using the same type of OAD-90 detectors equipped with various low-noise electret microphones (see Table 1, pos. 4–8). The experiments were carried out under laboratory conditions at room temperature. During the experiments, one OAD-90 detector in the optical scheme of the PA gas analyzer was successively replaced by another, equipped with a different type of microphones.

To select microphones, a sound microphone calibrator (NC-74 model) was used, which produced a standard sound signal (1 kHz frequency; 1 Pa sound pressure). The most sensitive samples were preliminarily selected from a series of studied microphones of various types (6…9 pcs. in a series), which were then installed (2 pcs.) in several modified OAD-90 detectors. For an objective assessment of the parameters of the studied microphones of various types, the measured signal (U_1) was recorded at the lowest resonant frequency (f_1) from only one of the microphones of differential OAD-90 detector; in this case, a differential amplifier was not used.

In the course of experiments with all OAD-90 detectors with various microphones under study, four fragments of responses with 30…60 sec duration each were sequentially recorded. First, the OAD-90 detector was filled with high-purity nitrogen (grade 5.6; purity – not less than

Table 1
Types and parameters of electret microphones used as part of the resonant differential OAD-90 detectors.

#	Microphone's model	Dimensions	Impedance	Response	SNR	Manufacturer
1	CME-1538-100LB	Ø4 × 1.5 mm	2200 ohm	–(38 ± 3) dB	More than 58 dB	CUI Devices
2	EM-6050	Ø6 × 5 mm	2200 ohm	–32…–44 dB	More than 60 dB	Soberton Inc.
3	WM-61A	Ø6 × 3.4 mm	2200 ohm	–(35 ± 4) dB	More than 62 dB	Panasonic Corporation
4	HBO0603H-50/1340	Ø6 × 2.7 mm	2200 ohm	–(30 ± 3) dB	76 dB	BeStar Technologies, Inc.
5	HBO0803A-48/1341	Ø8 × 3 mm	2200 ohm	–(28 ± 3) dB	78 dB	BeStar Technologies, Inc.
6	HBO1003D-46/1342	Ø9.7 × 5 mm	2200 ohm	–(26 ± 3) dB	80 dB	BeStar Technologies, Inc.
7	DOM-3027L-HD-R	Ø8 × 3 mm	2200 ohm	–(27 ± 3) dB	77 dB	PUI Audio, Inc.
8	AOM-5024L-HD-R	Ø9.7 × 5 mm	2200 ohm	–(24 ± 3) dB	80 dB	PUI Audio, Inc.

99.9996%; CH_4 admixture – not more than 1 ppm; moisture admixture – not more than 1.5 ppm), then with a test gas mixture (N_2 + 9.7 ppm CH_4), then the detector was purged with room air, then the detector was purged with air from the street. During the measurements, the pumping and purge of gas through the OAD-90 detectors under study was turned off, and the gas ports of the detectors (inlet/outlet) were closed. The QCL operated at the optimum operating temperature T_{QCL} = 28.2 °C with a pulse repetition frequency (f_{PRF}) equal to the lowest resonant frequency f_1 of the differential OAD-90 detector (measured automatically during the experiment at the beginning of each recording fragments). The average QCL radiation power was P_0= 25 mW.

The best results in terms of the threshold sensitivity of the PA methane sensor being developed were recorded when a microphone of HBO1003D-46/1342 model (see Table 1, pos. 6) was used as part of the measuring OAD-90 detector. Fig. 5 shows experimental recordings of signals from a microphone of this model (installed in one of the acoustic resonators of the differential OAD-90 detector), a sealed-off gas-filled PA *Ref*-cell, as well as readings of the PA methane sensor (ppm CH_4) when the measuring detector is successively filled with highly pure nitrogen, test gas mixture (N_2 + 9.7 ppm CH_4), room air and street air.

As can be seen from the graphs in Fig. 5a, when the resonant differential OAD-90 detector is filled with highly pure nitrogen, the average noise level of the PAD's microphone is $U_1(N_2)$ = (284.1 ± 99.63) nV (at bandwidth BP = 20 Hz). When the OAD-90 detector is filled with a test gas mixture (N_2 + 9.7 ppm CH_4) and then with room or street air, the signal from the microphone (U_1) increases by more than 100 times. It should be noted that in order to achieve the minimum level of background absorption in the measuring OAD-90 detector, it was necessary to blow it with pure nitrogen for a long time even after the detector was briefly filled with room air.

The signal from the microphone of the sealed-off gas-filled PA *Ref*-cell (see Fig. 5b) is practically constant in all fragments of the experimental recording and amounts to $U_2 \approx 1.5$ mV. Calibration of readings of the PA methane sensor against the test gas mixture N_2 + 9.7 ppm CH_4 (see Fig. 5c) showed that the recorded noise track when the measuring OAD-90 detector is filled with highly pure nitrogen corresponds to the equivalent background concentration $n_b(N_2)$ = (24.14 ± 8.46) ppb CH_4 (see also a similar fragment of the record in Fig. 6a: $n_b(N_2)$ = (26.64 ± 8.39) ppb CH_4). When the measuring OAD-90 detector is filled with room or street air, the background CH_4 concentration is n_2 = 2.91 ppm and n_3 = 2.63 ppm, respectively.

The ADC board intrinsic noise measured during the experiments was U_{noise}(ADC) ≈ (140 ± 44) nV (at bandwidth BP = 20 Hz; microphone is muted), which corresponds to the equivalent concentration n_{min}(ADC) ≈ (11.9 ± 3.7) ppb CH_4, i.e. almost ~2.3 times lower than the minimum background signal of the PA methane sensor (response to pure N_2).

The results of experiments with the PA methane sensor, carried out with the same type of measuring differential OAD-90 detectors, equipped with other models of low-noise electret microphones (see Table 1, pos. 4, 5, 8), are presented in Table 2.

As can be seen from Table 2, the readings of the PA methane sensor when the measuring OAD-90 detector is filled with street air for all the studied types of microphones are in a narrow range (n_3 = 2.61…2.66 ppm CH_4). At the same time, the background concentration of methane in the room air in all cases has a higher value (n_2 = 2.85…3.19 ppm CH_4), which can be explained by the presence of several people in the laboratory, as well as by purging the test gas mixture (N_2 + 9.7 ppm CH_4) from the high pressure cylinder through the measuring detector into the room atmosphere. It should be noted that the background concentration of methane in the air in a ventilated room decreases.

Using the value of CH_4 absorption coefficient measured earlier in our

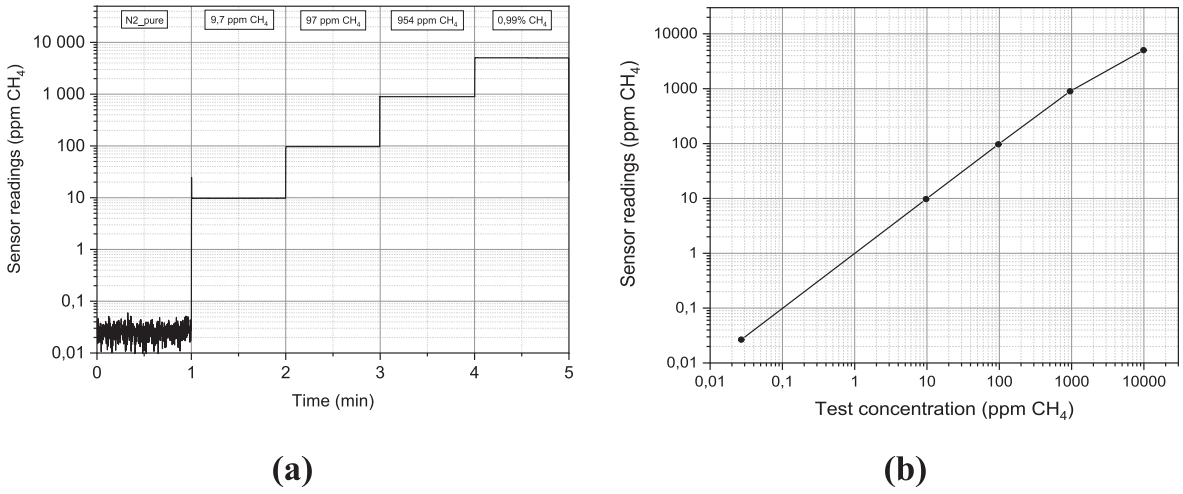

Fig. 6. (a) – Fragments of experimental records of the PA methane sensor readings for test gas mixtures with different concentrations of CH_4 impurity; **(b)** – Experimental dependence of PA sensor readings on test gas mixtures with different methane impurity contents in the range of ~10 ppm…1% CH_4, including high-purity nitrogen.

Table 2
Measured PA methane sensor data with using various models of low-noise electret microphones as part of the differential OAD-90 detector (at bandwidth $BP = 20$ Hz).

#	*Microphone's model*	*Response to high purity nitrogen (n_b)*	*Response to room air (n_2)*	*Response to street air (n_3)*	*Calibration mixture (n_1)*
1	HBO0603H-50/1340 (Ø6 mm)	(33.66 ± 11.25) ppb	2.91 ppm	2.63 ppm	N_2 + 9.7 ppm CH_4
2	HBO0803A-48/1341 (Ø8 mm)	(47.09 ± 11.25) ppb	3.19 ppm	2.61 ppm	N_2 + 9.7 ppm CH_4
3	HBO1003D-46/1342 (Ø9.7 mm)	(24.14 ± 8.46) ppb (see Fig. 5c)	2.85 ppm	2.66 ppm	N_2 + 9.7 ppm CH_4
		(26.64 ± 8.39) ppb (see Fig. 6a)	-	-	N_2 + 97 ppm CH_4
4	AOM-5024L-HD-R (Ø9.7 mm)	(38.43 ± 10.27) ppb	2.89 ppm	2.64 ppm	N_2 + 9.7 ppm CH_4

work [31] (k_{CH4}(7.652 μm) = 17.52 cm^{-1}·atm^{-1}), as well as the experimental data of this work ($P_0 = 25$ mW; (1σ) = 8.39 ppb CH_4; $BP = 20$ Hz), it is possible to determine the value of the normalized noise equivalent absorption of the developed PA methane sensor:

$(NNEA) = 8.22 \times 10^{-10}$ cm^{-1}·W/$Hz^{1/2}$.

Note that the minimum value of the equivalent normalized parameter (*NNEA*), limited by the intrinsic noise of the ADC, in our case reaches the value $(NNEA)_{ADC} \approx 3.62 \times 10^{-10}$ cm^{-1}·W/$Hz^{1/2}$.

Additionally, an experiment was carried out using a lock-in amplifier (Stanford SR830 DSP model), to which a signal was applied from PAD's microphone (HBO1003D-46/1342 model; Ø9.7 mm) when the measuring OAD-90 detector was filled with various gas mixtures (as in Fig. 5). The microphone was powered from a battery (6 VDC), the load resistance was 2.2 kOhm. The settings of the lock-in amplifier (integration time 1 s; filter slope 12 dB/octave; bandwidth $BP = 0.25$ Hz) are the same as in similar papers of other authors [25,27,51–53]. In this experiment, when the OAD-90 detector was filled with highly pure nitrogen, the minimum average level of the measured signal from the microphone was $U_1^*(N_2)$ = (1151.7 ± 38.6) nV, which significantly exceeds the previously measured value of the background signal using the "*ILPA*" program: $U_1(N_2) \approx$ (284.1 ± 99.63) nV (see Fig. 5a). After calibrating of the PA sensor response using a Stanford SR830 DSP lock-in amplifier, the measured background equivalent signal was $n_b^*(N_2; 1\ s)$ = (75.55 ± 2.53) ppb CH_4, which corresponds to the value of $(NNEA)^*$ = 2.2×10^{-9} cm^{-1}·W/$Hz^{1/2}$. When the measuring OAD-90 detector was filled with room or street air, the PA sensor readings were $n_2^* = 3.10$ ppm CH_4 and $n_3^* = 2.67$ ppm CH_4, respectively.

We also note that earlier in our paper [31], the measuring resonant differential OAD-90 detector was equipped with electret microphones of CME-1538-100LB model (SNR ~ 58 dB; see Table 1, pos. 1). Under the same experimental conditions, the average level of background measured data of the PA methane gas analyzer was reached when the measuring OAD-90 detector was filled with nitrogen $n_b(N_2; CME)$ = (307 ± 105) ppb CH_4 [31]. In this work, when using a low-noise HBO1003D-46/1342 electret microphone (SNR ~ 80 dB; see Table 1, pos. 6) as part of the OAD-90 detector, when the detector was filled with highly pure nitrogen, the average level of background of the PA sensor measured data was $n_b(N_2)$ = (26.64 ± 8.39) ppb CH_4. This value is ~11.5 times (by ~21 dB) lower than when using CME-1538-100LB microphones. It can be seen that the increase in the threshold sensitivity of the PA methane sensor occurred almost to the same extent as the change in the SNR of the microphones used in both cases (difference ~22 dB, see Table 1).

3.5. Determining the dynamic range of measurements

Experiments were carried out to determine the linear section of CH_4 concentration dynamic range measurements of the developed PA methane sensor using several nitrogen-based test gas mixtures with different methane impurity concentrations: 9.7 ppm; 97 ppm; 954 ppm; 0.99% CH_4. All gas mixtures are certified and are contained in standard high-pressure steel gas cylinders with a volume of 5 L.

Fig. 6a shows experimental recordings of readings fragments of the PA methane sensor (each lasting 1 min) when the measuring detector is filled with the test gas mixtures listed above, including high-purity nitrogen. The HBO1003D-46/1342 microphone (see Table 2, pos. 3) is installed in the OAD-90 detector. The PA methane sensor measured data were calibrated using a test gas mixture (N_2 + 97 ppm CH_4). The results of experimental investigation of the PA methane sensor (see Fig. 6a) are presented in Table 3, as well as in Fig. 6b in the form of a graph of the experimental dependence of the PA methane sensor readings on the concentration of CH_4 in the test gas mixtures.

The linear section of the experimental dependence of PA sensor readings on methane concentration in test gas mixtures is observed practically from ~25 ppb CH_4 (minimum average background signal) to ~800 ppm CH_4 (see Fig. 6b; Table 3); for higher methane concentrations, there is a noticeable deviation of PA sensor readings from the test concentration. This can be seen already when using the test gas mixture (N_2 + 954 ppm CH_4), for which the PA sensor readings are n_1 = (895.6 ± 0.2) ppm CH_4, which is ~6.1% lower than the test methane concentration. For another gas mixture (N_2 + 0.99% CH_4), this imbalance in the values of the test and measured CH_4 concentrations already reaches almost 50%. Such a noticeable difference is associated with an increase in the optical thickness of the measuring OAD-90 detector ($\tau_1 \geq 0.2$), when the weak absorption condition is violated and the function exp ($-\tau_1$) leaves the linear function approximation ~$(1 - \tau_1)$.

Thus, for this PA methane sensor, a linear section of the dynamic range of concentration measurement was obtained from ~25 ppb CH_4 to ~800 ppm CH_4, which exceeds 4 decades (the ratio of the extreme measured values of CH_4 concentration in the linear mode is $(n_{max}/n_{min}) \approx 3 \times 10^4$).

3.6. Comparison of the obtained results with the parameters of other PA methane gas analyzers

This section is devoted to compare the obtained results with the work

Table 3
PA methane sensor readings when using various test gas mixtures (at bandwidth $BP = 20$ Hz).

#	*Test gas mixture*	*PA methane sensor readings*	*Deviation from CH_4 test concentration*	*Note*
1	High purity nitrogen	(26.64 ± 8.39) ppb CH_4	–	Minimum background signal of the PA sensor readings
2	N_2 + 9.7 ppm CH_4	(9.74 ± 0.02) ppm CH_4	+0.4%	Linear section of the PA sensor calibration dependence
3	N_2 + 97 ppm CH_4	(96.99 ± 0.03) ppm CH_4	±0%	PA sensor calibration point
4	N_2 + 954 ppm CH_4	(895.6 ± 0.2) ppm CH_4	−6.1%	There is a slight deviation of PA sensor readings from the test value n_1
5	N_2 + 0.99% CH_4	(5031.9 ± 10.8) ppm	−49.2%	There is a strong deviation of PA sensor readings from the test value n_1

of other groups that do research in the field of laser PA spectroscopy. Table 4 presents the parameters of the best mid-IR laser PA gas analyzers implemented over the past ~30 years in various laboratories around the world using resonant longitudinal PADs (Harren's scheme) [57–59], resonant differential PADs (Miklos's scheme, Sherstov's scheme) [24,25,27,28,30,31,44–53,55], quartz tuning forks (QEPAS sensors) [60–64], cantilevers (CEPAS sensors) [65,66].

As can be seen from Table 4, the value of the normalized noise equivalent absorption (*NNEA*) measured by various authors for PA gas analyzers based on resonant differential PADs (OAD-90 detector) (see pos. 11–18) is in the range (*NNEA*) ≈ (0.83…3.32) × 10^{-9} cm^{-1}·W/$Hz^{1/2}$. For QEPAS sensors (see pos. 6, 8–10) the value of the normalized parameter is (*NNEA*) = (2.9…29) × 10^{-9} cm^{-1}·W/$Hz^{1/2}$.

Separately, we note the value of the normalized parameter (*NNEA*) = 2.7 × 10^{-10} cm^{-1}·W/$Hz^{1/2}$ (see Table 4, pos. 7), obtained in paper [61] for the QEPAS SF_6 sensor, which is clearly out of the general range of similar sensors based on quartz tuning forks. The article [61] describes in detail the conditions for the experiment on the detection of a small SF_6 impurity (ν = 948.62 cm^{-1}; P_0 = 18 mW (QCL); (1σ) = 50 ppt SF_6 (1 s); *BP* = 0.16675 Hz); (*NNEA*) = 2.7 × 10^{-10} cm^{-1} W/$Hz^{1/2}$), from which it is clear that to calculate the parameter value (*NNEA*) the absorption coefficient k_{SF6}(948.62 cm^{-1}) ≈ 120 cm^{-1}·atm^{-1} was used (probably taken from the HITRAN spectral database [18]: at the specified frequency k_{SF6}(HITRAN) ≈ 100 cm^{-1}·atm^{-1}), which is an error. The paper [67] presents the results of experimental measurement of SF_6 absorption coefficient in the spectral range 936…954 cm^{-1}, where it is shown that at a frequency ν = 948.62 cm^{-1} (as in article [61]) the absorption coefficient k_{SF6}* ≈ 322 cm^{-1}·atm^{-1}, which differs from the data of the HITRAN spectral database by more than 3 times. When using this experimentally measured value of k_{SF6}*(948.62 cm^{-1}), the calculated value of the normalized parameter in [61] (see Table 4, pos. 7) will be (*NNEA*)* ≈ 7.1 × 10^{-10} cm^{-1}·W/$Hz^{1/2}$, which is quite close to the value of the parameter (*NNEA*) obtained in this paper (see Table 4, pos. 18).

Note that the placement of PA detectors inside high-*Q* optical cavities noticeably increases the threshold sensitivity of PA gas analyzers (see [57,58]). For example, in [68], a resonant longitudinal windowless PAS cell (length 42 mm; f_1 = 3986 Hz; *Q* ~ 15.5) was placed in a high-*Q* optical cavity for NH_3 detection. A widely tunable EC-QCL (λ ≈ 10.35 μm) was used. The radiation power inside the optical cavity reached 9.6 W. As a result, the experimentally measured values of n_{min} ≈ 10 ppb NH_3 and (*NNEA*) = 1.1 × 10^{-11} cm^{-1} W/$Hz^{1/2}$ was achieved.

In [69], the high finesse bow-tie optical cavity coupled with CW-QCL (ν ≈ 2311 cm^{-1}) and intra-cavity QEPAS sensor was used for ultra-sensitive CO_2 detection. A power enhancement factor of 240 was achieved, corresponding to intra-cavity power of 0.72 W. A minimum detection limit of 300 pptV CO_2 at a total gas pressure of 50 mbar was measured with a 20 s integration time; parameter (*NNEA*) = 3.2 × 10^{-10} cm^{-1} W/$Hz^{1/2}$.

In [70], for detecting C_2H_2 using a DFB laser (λ = 1530 nm), the authors placed the CEPAS detector in a high-*Q* optical resonator to increase the optical power (by about 100 times), which led to a sensitivity of n_{min} = 75 ppt C_2H_2 (10 s) and an exceptionally high value of (*NNEA*) = 1.75 × 10^{-12} W·cm^{-1}/$Hz^{1/2}$.

At the end of Table 4 (see pos. 21–28), the parameters of some implemented airmobile methane sensors also shows, the sensitivity of which is in the range of ~1…10 ppb CH_4. These sensors use various absorption detection methods (TDLS, ICOS, CRDS, multi-pass cells, etc.), however, the methane sensor considered in this work is probably the first of the photo-acoustic gas analyzers developed for use on UAVs.

Thus, the laser PA methane sensor based on QCL (~7.65 μm), resonant differential detector (OAD-90), and sealed-off gas-filled PA *Ref*-cell studied in this work is currently one of the highly sensitive CH_4 PA gas analyzers for use at UAVs. Comparison of the results of various papers (see Table 4) showed that mid-IR laser PA gas analyzers based on the resonant differential OAD-90 detector practically are in no way inferior, and in some cases exceed the threshold sensitivity of PA methane sensors built using the QEPAS technology with quartz tuning forks, as was noted in [27].

4. Development of airborne laser PA methane sensor

Based on the experimental results described above, an instrumental version of the laser PA methane sensor has been developed, adapted for installation on UAV's board (like [32–42]). The structure of the developed PA methane sensor is shown in Fig. 7a. It practically repeats the scheme of the experimental setup (see Fig. 1). The main optical units of the PA methane sensor are QCL (λ ≈ 7.65 μm), resonant differential detector (OAD-90 model), sealed-off gas-filled PA *Ref*-cell, and power meter (MG-30 pyrodetector). The operating procedure of the PA methane sensor and the algorithm for measuring the CH_4 concentration in the analyzed air sample pumped through the measuring OAD-90 detector are described above.

The QCL operates in a repetitively pulsed mode at a wavelength of λ = 7.652 μm, corresponding to the CH_4 absorption peak near ~7.7 μm. The QCL operating temperature is maintained by laser's thermostat and thermal controller. The operating current and repetition rate of QCL radiation pulses are set by the laser power supply (see Fig. 7a). The pump provides air pumping through the measuring OAD-90 detector at a rate of ~0.5 L/min (laminar flow). The acoustic muffler is designed to suppress pressure fluctuations that occur when the air pump is operating in the mode of pumping air through the measuring detector.

The analyzed air sample enters the measuring OAD-90 detector through a long sampling hose (up to ~3…6 m) with a filter and a sinker at the end. Such scheme for delivering an air sample for analysis was proposed to exclude the influence of a downward air flow from the UAV's propellers (see [71,72]). Note that in [73] the downdraft air field of a UAV (JF01-10 model; 6 propellers) was simulated and showed that a suitable operating hover height for this UAV is ~3 m. In extreme cases, air for analysis can be taken from a region slightly above the plane of the UAV propellers (see [74]).

The controller of PA methane sensor measures the lowest resonant frequency (f_1) of the OAD-90 detector, sets the QCL pulse repetition frequency (f_{PRF}) equal to the resonant frequency f_1, collects and processes signals from the microphones of the differential OAD-90 detector, sealed-off gas-filled PA *Ref*-cell, pyrodetector, calculates CH_4 concentration in the analyzed air sample, transmits the processed information to the main controller, controls the on/off of the light indicators informing the operator about the functional state of the PA methane sensor during operation.

The PA methane sensor is controlled from the main controller (see Fig. 7b) installed on the UAV's board, which receives and transmits information to the operator's computer via a radio channel. Topographic reference to the terrain is carried out using a GLONASS/GPS sensor. The PA methane sensor is powered from an external source (battery) with a voltage of 9…60 VDC (optimally 24…27 VDC), power consumption does not exceed 20 VA.

Note that the use of a small-sized sealed-off gas-filled PA *Ref*-cell (external dimensions ~Ø13 × 18 mm, including windows; see Fig. 2c) in the design of this PA methane sensor for normalization of absorption signals in the measuring PAD practically replaces the auxiliary part of some QEPAS sensors for tuning to the center of the absorption band of the studied gas (see [60–62]), which includes a simple gas-filled *Ref*-cell (5…10 cm long) and a photodetector. In our case, a small-sized sealed-off gas-filled PA *Ref*-cell is a simpler and cheaper solution.

Fig. 8 shows photographs of the manufactured airborne laser PA methane sensor. The hermetically sealed case of the rectangular device has dimensions of 315 × 165 × 110 mm, assembled from aluminum plates of various thicknesses, connected by screws, the joints between the plates and the threads of the screws are treated with sealant during assembly. Removable covers of the device (front and top) are sealed with a rubber cord of round section, laid in technological grooves.

On the front panel of the PA methane sensor there are electrical and

Table 4
Summary table of various mid-IR PA gas analyzers parameters.

#	Authors, year, Ref.	Detector type	Gas	Radiation source	Resonant frequency, f_1	*NNEA* [cm^{-1}·W $Hz^{-1/2}$]	Threshold sensitivity
1	Harren, et al. (1990) [57]	Harren's (Ø6 × 100 mm + Ø20 × 50 mm)	C_2H_4	CO_2 laser $\nu = 949.479\ cm^{-1}$ $P_{intra} = 100$ W	1653 Hz ($Q = 32$)	–	$(1\sigma) = 1.8 \times 10^{-10}\ cm^{-1}$ ($n_{min} \approx 6$ ppt C_2H_4)
2	Fink, et al. (1996) [58]	Harren's	C_2H_4	CO_2 laser $\nu = 949.479\ cm^{-1}$ $P_{intra} = 40$ W	–	–	$(1\sigma) = 3 \times 10^{-10}\ cm^{-1}$ ($n_{min} \approx 11$ ppt C_2H_4)
3	Herpen, et al. (2002) [59]	Harren's (Ø6 × 100 mm + Ø20 × 50 mm)	C_2H_6	OPO (PPLN) $\nu = 2996.9\ cm^{-1}$ $P_0 = 2.2$ W	1653 Hz ($Q = 32$)	–	$(1\sigma) = 3.3 \times 10^{-10}\ cm^{-1}$ ($n_{min} \approx 10$ ppt C_2H_6)
4	Miklos, et al. (2001) [55]	Miclos's (Ø5.5 × 40 mm + Ø20 × 20 mm)	CH_4 C_2H_4 NH_3	$P_0 = 1$ W	~4000 Hz	- - -	$(1\sigma) = 1 \times 10^{-9}\ cm^{-1}$
5	Miclos, et al. (2002) [24]	Miclos's (Ø5.5 × 40 mm + Ø20 × 20 mm)	CH_4	OPO (PPLN-GIOPO) $\nu = 2948\ cm^{-1}$ $P_0 = 60$ mW	4100 Hz ($Q = 17$)	~1.1×10^{-9} *	$(1\sigma) = 1 \times 10^{-9}\ cm^{-1}$ (1 s) ($n_{min} = 1.2$ ppbV CH_4)
6	Kosterev, et al. (2008) [60]	QEPAS	CH_4	$\nu = 6057.1\ cm^{-1}$	32 kHz	2.9×10^{-8}	$n_{min}(CH_4) = 66$ ppbV·W/$Hz^{1/2}$
7	Spagnolo, et al. (2012) [61]	QEPAS	SF_6	948.62 cm^{-1} (QCL) $P_0 = 18$ mW	32 kHz	2.7×10^{-10} ~7.1×10^{-10} *	$(1\sigma) = 50$ ppt SF_6 (1 s) ($BP = 0.16675$ Hz)
8	Sampaolo, et al. (2016) [62]	QEPAS	SF_6	947.93 cm^{-1} (QCL) $P_0 = 25$ mW	32 kHz	~2.5×10^{-7} *	$(1\sigma) = 2.75$ ppb SF_6 (1 s) ($BP = 0.16675$ Hz)
9	Wu, et al. (2019) [63]	QEPAS	CH_4	$\lambda_2 = 3.3$ μm (ICL) $P_2 = 5.2$ mW	$f_1 = 2868$ Hz $f_2 = 17741$ Hz	2.9×10^{-9}	$(1\sigma) = 50$ ppb CH_4 (1 s) ($BP = 0.833$ Hz)
10	Menduni, et al. (2023) [64]	QEPAS	CH_4 N_2O NH_3	1275.04 cm^{-1} (74 mW) 1275.49 cm^{-1} (77 mW) 1103.44 cm^{-1} (59 mW)	12.467 kHz ($Q = 13180$)	~6.4×10^{-9} * ~3.8×10^{-9} * ~2.1×10^{-9} *	$(1\sigma) = 28$ ppb CH_4 (0.1 s) $(1\sigma) = 9$ ppb N_2O (0.1 s) $(1\sigma) = 6$ ppb NH_3 (0.1 s)
11	Sherstov, et al. (2017) [46]	OAD-90 (Ø9 × 90 mm + Ø20 × 8 mm)	SF_6	CO_2 laser $\lambda \approx 10.5 \ldots 10.6$ μm $P_0 = 250$ mW	1750 Hz ($Q \approx 54$)	~2.9×10^{-9} *	$n_b \approx 100$ ppt SF_6 (0.1 s)
12	Zheng, et al. (2017) [25]	OAD-90 (Ø8 × 90 mm + Ø20 × 10 mm)	CH_4	$\lambda = 3.2$ μm (ICLED) $P_0 \approx 0.7$ mW	1799 Hz	~1.5×10^{-7} *	$(1\sigma) = 3.6$ ppmV CH_4 (1 s) (12 dB/oct; $BP = 0.25$ Hz)
13	Yin, et al. (2017) [51]	OAD-90 (Ø8 × 90 mm + Ø20 × 10 mm)	NO_2	$\lambda = 447$ nm $P_0 = 3.5$ W	1752 Hz	1.583×10^{-9}	$(1\sigma) \approx 54$ pptV NO_2 (1 s) (12 dB/oct; $BP = 0.25$ Hz)
14	Yin, et al. (2017) [52]	OAD-90 (Ø8 × 90 mm + Ø20 × 10 mm)	SO_2	$\lambda = 303.6$ nm $P_0 = 5$ mW	1783 Hz (N_2) 683.6 Hz (SF_6)	1.15×10^{-9}	$(1\sigma) = 74$ ppbV SO_2 (1 s) (12 dB/oct; $BP = 0.25$ Hz)
15	Yin, et al. (2020) [53]	OAD-90 (Ø8 × 90 mm + Ø20 × 10 mm)	SO_2	$\lambda = 7.41$ μm (QCL) $P_0 \approx 30$ mW	1780 Hz	3.32×10^{-9}	$(1\sigma) = 2.45$ ppb SO_2 (1 s) (12 dB/oct; $BP = 0.25$ Hz)
16	Zheng, et al. (2020) [27]	OAD-90 (Ø8 × 90 mm + Ø20 × 10 mm)	CH_4	$\lambda = 3.3$ μm (ICL) $P_0 = 9.6$ mW	1800 Hz	1.23×10^{-9}	$(1\sigma) \approx 4.35$ ppb CH_4 (1 s) (12 dB/oct; $BP = 0.25$ Hz) $(1\sigma) = 0.6$ ppb CH_4 (90 s)
17	Sherstov, Vasiliev (2021) [50]	OAД-90 (Ø9 × 90MM + Ø20 × 8MM)	SF_6	CO_2 laser $\lambda \approx 10.5 \ldots 10.6$ μm $P_0 = 250$ mW	1750 Гц ($Q \approx 54$)	~2.9×10^{-9} *	$n_b \approx (0.64 \pm 0.13)$ ppb SF_6 (0.1 s) $(1\sigma) \approx 10$ ppt SF_6 (10 s)
18	Sherstov, et al. (2023) [This article]	OAD-90 (Ø9 × 90 mm + Ø20 × 8 mm)	CH_4	$\lambda = 7.652$ μm (QCL) $P_0 = 25$ mW	1750 Hz ($Q \approx 54$)	8.22×10^{-10}	$n_b \sim (26.64 \pm 8.39)$ ppb CH_4 ($BP = 20$ Hz) $(1\sigma) \approx 2.5$ ppb CH_4 (1 s)
19	Koskinen, et al. (2007) [65]	CEPAS	CO_2	$\lambda = 1572$ nm (DFB) $P_0 = 30$mW	20 Hz	1.7×10^{-10}	$(1\sigma) = 1.9$ ppm (2.6 s)
20	Tomberg, et al. (2018) [66]	CEPAS (PA-201)	HF	PPLN-OPO $\lambda = 2475$ nm $P_0 = 950$ mW	–	5.19×10^{-10}	$(1\sigma) = 2.5$ ppt (15 s)
21	Khan, et al. (2012) [32] **	TDLS (18 m)	CH_4	$\lambda = 1653$ nm	–	–	$(1\sigma) \approx 2$ ppb CH_4 (1 s)
22	Berman, et al. (2012) [33] **	ICOS	CH_4 CO_2 H_2O	$\lambda_1 = 1650$ nm $\lambda_2 = 1603$ nm $\lambda_3 = 1603$ nm	–	–	$(1\sigma) = 1.7$ ppb CH_4
23	Nathan, et al. (2015) [34] **	Herriott (20 m)	CH_4	$\lambda = 1651$ nm	50 kHz/50 Hz	–	$(1\sigma) \approx 0.1$ ppm CH_4 (1 s)
24	Golston, et al. (2017) [35] **	Herriott	CH_4	$\lambda = 3.27$ μm	–	–	$(1\sigma) \approx 5$–10 ppb CH_4 (1 s)
25	Brosy, et al. (2017) [36] **	CRDS (Picarro)	CH_4	–	–	–	$(1\sigma) \approx 7$ ppb CH_4
26	Martinez, et al. (2020) [39] **	CRDS	CH_4	$\lambda = 1651$ nm $P_0 = 5$ mW	350–500 Hz	–	$(1\sigma) \approx 10$–30 ppb CH_4 (1 s)
27	Tuzson, et al. (2020) [40] **	Multipass cell	CH_4	$\lambda = 7.83$ μm (QCL)	~570 Hz	–	$(1\sigma) \approx 1.1$ ppb CH_4 (1 s)
28	Shah, et al. (2020) [41] **	ICOS	CH_4	$\lambda = 1651$ nm	–	–	$(1\sigma) \approx 0.71$ ppb CH_4 (1 s)

* Values calculated by the authors of this article.
** Laser gas analyzers placed on UAV or aircraft.

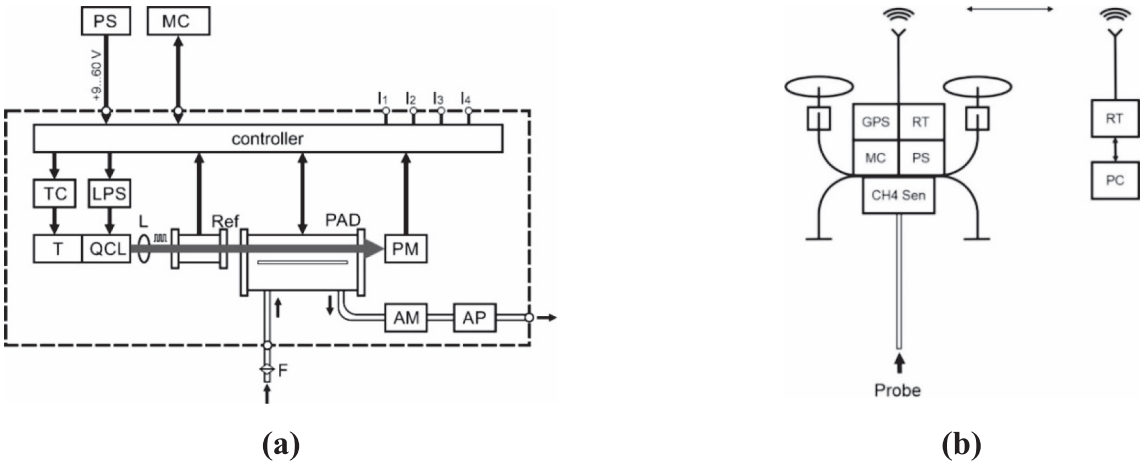

Fig. 7. **(a)** – The structure of laser PA methane sensor: *PS* – power supply; *MC* – main controller; I_1-I_4 – color light indicators; *TC* – thermal controller; *LPS* – laser power supply; *T* – thermostat; *QCL* – quantum-cascade laser; *L* – lens; *Ref* – gas-filled cell; *PAD* – photo-acoustic detector; *PM* – power meter; *AM* – acoustic muffler; *AP* – air pump; **(b)** – Scheme of practical use of PA methane sensor on UAV's board: *GPS* – position sensor; *RT* – radio transceiver; *CH4 Sen* – laser PA methane sensor; *PC* – operator's computer; *Probe* – analyzed air sample.

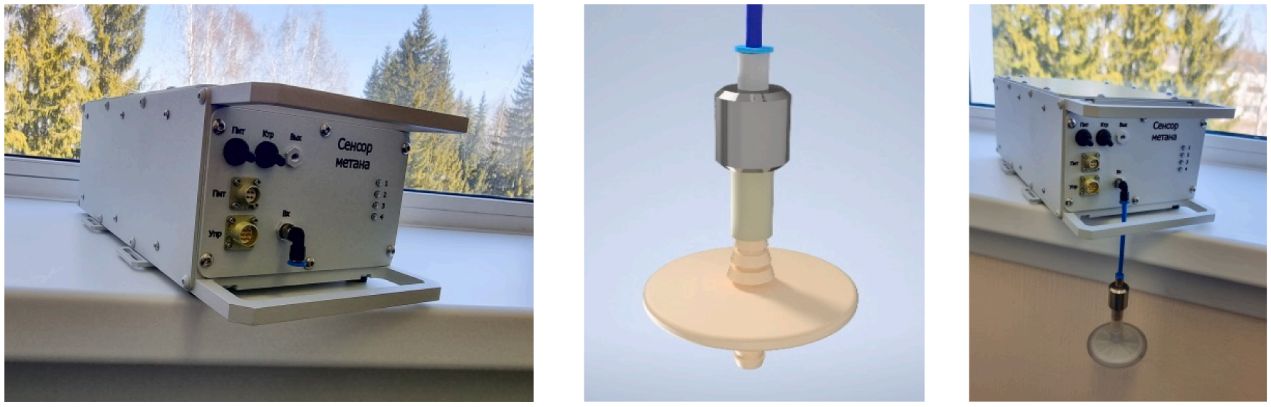

Fig. 8. **(a)** – External view of the airborne laser PA methane sensor; **(b)** – The device of the input aerosol filter with a sinker; **(c)** – PA methane sensor in the equipped state with an attached sampling hose (up to 3…6 m long) with a filter and a sinker at the end. On the bottom of the PA methane sensor, special eyelets are installed for attaching the device with straps to the bottom of the UAV.

gas connectors, toggle switches, light indicators. For carrying the device, strong handles protruding forward are provided, which protect the electrical connectors from mechanical damage. Excess heat generated by the laser's thermostat is removed to the rear wall of the instrument. Rubber feet are installed on the bottom and rear wall of the case. Special eyelets are also provided on the bottom of the device for fixing the PA methane sensor on the UAV's board using straps. The mass of the assembled instrument is ~3.1 kg. In addition, the operation of this PA methane sensor in manual mode is provided using a previously developed manual control panel from the SF_6 PA leak detector "KARAT" [50].

During preliminary tests, the developed PA methane sensor showed operability in the temperature range of +5…+45 °C. At present, the PA methane sensor is being prepared for testing in the field conditions, including when used on the UAV's board, as well as in manual mode using a remote hand-held control panel.

5. Conclusion

A compact highly sensitive laser PA methane sensor based on quantum-cascade laser, resonant differential PAD, and sealed-off gas-filled PA *Ref*-cell has been developed. The QCL operates in a repetitively pulsed mode at a wavelength $\lambda = 7.652$ μm corresponding to CH_4 absorption peak. The QCL pulse repetition frequency is equal to the lowest resonant frequency of the differential PAD (~1750…1780 Hz). The average QCL radiation power is 25 mW. The absorption signals in the measuring PAD are normalized according to the absorption signals in the sealed-off gas-filled PA *Ref*-cell, which significantly reduces the measurement errors of the CH_4 concentration when the laser radiation wavelength is unstable.

The threshold sensitivity of the laser PA methane sensor was studied using various types of low-noise electret microphones as part of a resonant differential detector (OAD-90 model). During the experiments, the minimum measured background signal of the PA sensor (with pure nitrogen) reached $n_b(N_2) = (26.64 \pm 8.39)$ ppb CH_4 (at a bandwidth of 20 Hz), which corresponds to the $(NNEA) = 8.22 \times 10^{-10}$ $cm^{-1} \cdot W/Hz^{1/2}$. It is shown that the intrinsic noise of the PA methane sensor (with pure nitrogen) is only ~2.3 times higher than the intrinsic noise of the electronic acquisition system.

The laser PA methane sensor studied in this work is currently one of the highly sensitive CH_4 PA gas analyzers. It is shown that mid-IR laser PA gas analyzers based on the resonant differential OAD-90 detector are in no way inferior, and in some cases exceed the threshold sensitivity of PA methane sensors built according to the QEPAS technology using quartz tuning forks.

An instrumental version of laser PA methane sensor adapted for placement on the UAV's board has been developed. The developed airborne laser PA methane sensor has dimensions of 315 × 165 × 110 mm, weight ~3.1 kg, power supply from an external source (battery; 9…60 VDC), power consumption ~20 VA. Currently, a prototype of PA methane sensor is being prepared for testing in the field conditions, including when used on the UAV's board.

Declaration of Competing Interest

The authors declare the following financial interests/personal relationships which may be considered as potential competing interests: Igor V. Sherstov has patent #Resonant Differential Optical-Acoustic Detector, Russian Patent RU 2761906 (2021) issued to Patentee.

Data availability

No data was used for the research described in the article.

Acknowledgements

This paper is dedicated to the memory of our dear colleague and friend Dmitry Kolker who sadly passed away last year. He devoted about 30 years of his life to the development of different radiation sources for gas analytical systems. The authors express their sincere gratitude to A. V. Kirpichnikov and N.L. Kvashnin (both - ILP SB RAS) for their help in the preparation of scientific equipment for some experiments, R.V. Pustovalova (ILP SB RAS) for assembling sealed-off gas-filled PA *Ref*-cells and designing some drawings.

This research was carried out with financial support from the Russian Science Foundation (Project 17-72-30006).

References

[1] L.E. Tuck, C. Samson, J. Laliberté, M. Cunningham, Magnetic interference mapping of four types of unmanned aircraft systems intended for aeromagnetic surveying, Geosci. Instrum. Method. Data Syst. 10 (1) (2021) 101–112, https://doi.org/10.5194/gi-10-101-2021.

[2] Real-time and historical methane CH_4 levels: https://www.methanelevels.org (Cited: June 3, 2023).

[3] S. Kirschke, P. Bousquet, P. Ciais, G. Zeng, et al., Three decades of global methane sources and sinks, Nat. Geosci. 6 (10) (2013) 813–823, https://doi.org/10.1038/ngeo1955.

[4] T.F. Villa, F. Gonzalez, B. Miljievic, Z.D. Ristovski, L. Morawska, An overview of small unmanned aerial vehicles for air quality measurements: Present applications and future prospectives, Sensors 16 (2016) 1072, https://doi.org/10.3390/s16071072.

[5] D.O. Sparkman Z, Penton., F.G. Kitson, Gas Chromatography and Mass Spectrometry: A practical guide (Academic Press, 2011), ISBN 978-0-08-092015-3.

[6] H.J. Hübschmann, Handbook of GC-MS: Fundamentals and Applications, third ed., John Wiley & Sons, 2015.

[7] D.R. Herriott, H.J. Schulte, Folded optical delay lines, Appl. Opt. 4 (8) (1965) 883–889, https://doi.org/10.1364/AO.4.000883.

[8] P. Werle, F. Slemr, K. Maurer, R. Kormann, R. Mücke, B. Jänker, Near- and mid-infrared laser-optical sensors for gas analysis, Optics and Lasers in Engineering (Elsevier BV) 37 (2–3) (2002) 101–114, https://doi.org/10.1016/s0143-8166(01)00092-6. ISSN 0143-8166.

[9] A.I. Nadezhdinskii, Y.Y. Ponurovskii, Diode laser spectrometer for high-precision measurements, Quantum Electron. 49 (7) (2019) 613–622, https://doi.org/10.1070/QEL16776.

[10] G. Berden, R. Engeln, Cavity Ring-Down Spectroscopy: Techniques and Applications, Wiley, Chichester, 2009, DOI: 10.1002/9781444308259.

[11] B. Henderson, A. Khodabakhsh, M. Metsälä, I. Ventrillard, F.M. Schmidt, D. Romanini, G.A.D. Ritchie, S.L. Hekkert, R. Briot, T. Risby, N. Marczin, F.J. M. Harren, S.M. Cristescu, Laser spectroscopy for breath analysis: towards clinical implementation, Appl. Phys. B 124 (2018) 161, https://doi.org/10.1007/s00340-018-7030-x.

[12] P.I. Abramov, E.V. Kuznetsov, L.A. Skvortsov, M.I. Skvortsova, Quantum-cascade lasers in medicine and biology (Review), J. Appl. Spectrosc. 86 (1) (2019) 1–26, https://doi.org/10.1007/s10812-019-00775-8.

[13] E. Zanzottera, Differential absorption lidar techniques in the determination of trace pollutants and physical parameters of the atmosphere, Crit. Rev. Anal. Chem. 21 (4) (1990) 279–319, https://doi.org/10.1080/10408349008051632.

[14] F.J.M. Harren, S.M. Cristescu, Photoacoustic Spectroscopy in Trace Gas Monitoring, Encyclopedia of Analytical Chemistry, John Wiley & Sons, Ltd., 2019, doi: 10.1002/9780470027318.a0718.pub3.

[15] P. Patimisco, V. Spagnolo, Quartz-Enhanced Photoacoustic Spectroscopy for Trace Gas Sensing (Encyclopedia of Analytical Chemistry: Applications, Theory and Instrumentation, Wiley Online Library (2021), https://doi.org/10.1002/9780470027318.a9760.

[16] Y. Yin, D. Ren, C. Li, R. Chen, J. Shi, Cantilever-enhanced photoacoustic spectroscopy for gas sensing: A comparison of different displacement detection methods, Photoacoustics 28 (2022), 100423, https://doi.org/10.1016/j.pacs.2022.100423.

[17] NIST Standard Reference Database: http://webbook.nist.gov/chemistry/ (Cited: June 3, 2023).

[18] L.S. Rothman, I.E. Gordon, et al., The HITRAN 2012 molecular spectroscopic database, J. Quant. Spectrosc. Radiat. Transf. 130 (2013) 4–50, https://doi.org/10.1016/j.jqsrt.2013.07.002.

[19] A. Nadezhdinskii, A. Berezin, S. Chernin, O. Ershov, V. Kutnyak, High sensitivity methane analyzer based on tuned near infrared diode laser, Spectrochim. Acta A 55 (10) (1999) 2083–2089, https://doi.org/10.1016/S1386-1425(99)00080-3.

[20] V.A. Kapitanov, I.S. Tyryshkin, N.P. Krivolutskii, Y.N. Ponomarev, M. De Batist, R. Y. Gnatovsky, Spatial distribution of methane over Lake Baikal surface, Spectrochim. Acta A 66 (4–5) (2007) 788–795, https://doi.org/10.1016/j.saa.2006.10.036.

[21] V.A. Kapitanov, Yu.N. Ponomarev, I.S. Tyryshkin, A.P. Rostov, Two-channel opto-acoustic diode laser spectrometer and fine structure of methane absorption spectra in 6070–6180 cm^{-1} region, Spectrochim. Acta A 66 (4–5) (2007) 811–818, https://doi.org/10.1016/j.saa.2006.10.046.

[22] J. Wang, H. Wang, X. Liu, A portable laser photoacoustic methane sensor based on FPGA, Sensors (Basel) 16 (9) (2016) 1551, https://doi.org/10.3390/s16091551.

[23] K.L. Moskalenko, A.I. Nadezhdinskii, E.V. Stepanov, Tunable diode laser spectroscopy application for ammonia and methane content measurements in human breath, Proc. SPIE 2205 (1994) 448–452, https://doi.org/10.1117/12.166259.

[24] A. Miklós, C.-H. Lim, W.-W. Hsiang, G.-C. Liang, A.H. Kung, A. Schmohl, P. Hess, Photoacoustic measurement of methane concentrations with a compact pulsed optical parametric oscillator, Appl. Opt. 41 (15) (2002) 2985–2993, https://doi.org/10.1364/AO.41.002985.

[25] H. Zheng, M. Lou, L. Dong, H. Wu, W. Ye, X. Yin, C.S. Kim, M. Kim, W.W. Bewley, C.D. Merritt, C.L. Canedy, M.V. Warren, I. Vurgaftman, J.R. Meyer, F.K. Tittel, Compact photoacoustic module for methane detection incorporating interband cascade light emitting device, Opt. Express 25 (14) (2017) 16761–16770, https://doi.org/10.1364/OE.25.016761.

[26] L. Lamard, D. Balslev-Harder, A. Peremans, J.C. Petersen, M. Lassen, Versatile photoacoustic spectrometer based on a mid-infrared pulsed optical parametric oscillator, Appl. Opt. 58 (2) (2019) 250–256, https://doi.org/10.1364/AO.58.000250.

[27] H. Zheng, Y. Liu, H. Lin, R. Kan, P. Patimisco, A. Sampaolo, M. Giglio, W. Zhu, J. Yu, F.K. Tittel, V. Spagnolo, Z. Chen, Sub-ppb-level CH_4 detection by exploiting a low-noise differential photoacoustic resonator with a room-temperature interband cascade laser, Opt. Express 28 (13) (2020) 19446–19456, https://doi.org/10.1364/OE.391322.

[28] M.V. Rocha, M.S. Sthel, M.G. Silva, L.B. Paiva, F.W. Pinheiro, A. Miklòs, H. Vargas, Quantum-cascade laser photoacoustic detection of methane emitted from natural gas powered engines, Appl. Phys. B 106 (3) (2012) 701–706, https://doi.org/10.1007/s00340-011-4800-0.

[29] M. Giglio, A. Zifarelli, A. Sampaolo, G. Menduni, A. Elefante, R. Blanchard, C. Pfluegl, M.F. Witinski, D. Vakhshoori, H. Wu, V.M.N. Passaro, P. Patimisco, F. K. Tittel, L. Dong, V. Spagnolo, Broadband detection of methane and nitrous oxide using a distributed-feedback quantum cascade laser array and quartz-enhanced photoacoustic sensing, Photoacoustics 17 (2020), 100159, https://doi.org/10.1016/j.pacs.2019.100159.

[30] I.V. Sherstov, D.B. Kolker, Photoacoustic methane gas analyser based on a 3.3-μm optical parametric oscillator, Quantum Electron. 50 (11) (2020) 1063–1067, https://doi.org/10.1070/QEL17316.

[31] I.V. Sherstov, D.B. Kolker, A.A. Boyko, V.A. Vasiliev, R.V. Pustovalova, Methane photo-acoustic gas analyzer based on 7.7-μm quantum cascade laser, Infrared Phys. Technol. 117 (2021) 103858, https://doi.org/10.1016/j.infrared.2021.103858.

[32] A. Khan, D. Schaefer, L. Tao, D.J. Miller, K. Sun, M.A. Zondlo, W.A. Harrison, B. Roscoe, D.J. Lary, Low Power Greenhouse Gas Sensors for Unmanned Aerial Vehicles, Remote Sens. 4 (5) (2012) 1355–1368, https://doi.org/10.3390/rs4051355.

[33] E.S.F. Berman, M. Fladeland, J. Liem, R. Kolyer, M. Gupta, Greenhouse gas analyzer for measurements of carbon dioxide, methane, and water vapor aboard an unmanned aerial vehicle, Sens. Actuators B 169 (2012) 128–135, https://doi.org/10.1016/j.snb.2012.04.036.

[34] B.J. Nathan, L.M. Golston, A.S. O'Brien, K. Ross, W.A. Harrison, L. Tao, D.J. Lary, D.R. Johnson, A.N. Covington, N.N. Clark, M.A. Zondlo, Near-Field Characterization of Methane Emission Variability from a Compressor Station Using a Model Aircraft, Environ. Sci. Tech. 49 (2015) 7896–7903, https://doi.org/10.1021/acs.est.5b00705.

[35] L.M. Golston, L. Tao, C. Brosy, K. Schäfer, B. Wolf, J. McSpiritt, B. Buchholz, D. R. Caulton, D. Pan, M.A. Zondlo, D. Yoel, H. Kunstmann, M. McGregor, Lightweight mid-infrared methane sensor for unmanned aerial systems, Appl. Phys. B 123 (2017) 170, https://doi.org/10.1007/s00340-017-6735-6.

[36] C. Brosy, K. Krampf, M. Zeeman, B. Wolf, W. Junkermann, K. Schäfer, S. Emeis, H. Kuntsmann, Simultaneous multicopter-based air sampling and sensing of meteorological variables, Atmos. Meas. Tech. 10 (2017) 2773–2784, https://doi.org/10.5194/amt-10-2773-2017.

[37] S. Yang, R.W. Talbot, M.B. Frish, L.M. Golston, N.F. Aubut, M.A. Zondlo, C. Gretencord, J. McSpiritt, Natural gas fugitive leak detection using an unmanned aerial vehicle: Measurement system description and mass balance approach, Atmos. 9 (2018) 383, https://doi.org/10.3390/atmos9100383.

[38] T.E. Barchyn, C.H. Hugenholtz, S. Myshak, J. Bauer, A UAV-based system for detecting natural gas leaks, J. Unmanned Veh. Syst. 6 (2018) 18–30, https://doi.org/10.1139/juvs-2017-0018.

[39] B. Martinez, T.W. Miller, A.P. Yalin, Cavity Ring-Down methane sensor for small unmanned aerial systems, Sensors 20 (2020) 454, https://doi.org/10.3390/s20020454.

[40] B. Tuzson, M. Graf, J. Ravelid, P. Scheidegger, A. Kupferschmid, H. Looser, R. P. Morales, L. Emmenegger, A compact QCL spectrometer for mobile, high-precision methane sensing aboard drones, Atmos. Meas. Tech. 13 (2020) 4715–4726, https://doi.org/10.5194/amt-13-4715-2020.

[41] A. Shah, J.R. Pitt, H. Ricketts, J.B. Leen, P.I. Williams, K. Kabbabe, M.W. Gallagher, G. Allen, Testing the near-field Gaussian plume inversion flux quantification, technique using unmanned aerial vehicle sampling, Atmos. Meas. Tech. 13 (2020) 1467–1484, https://doi.org/10.5194/amt-13-1467-2020.

[42] J.T. Shaw, A. Shah, H. Yong, G. Allen, Methods for quantifying methane emissions using unmanned aerial vehicles: a review, Phil. Trans. R. Soc. A 379 (2021) 20200450, https://doi.org/10.1098/rsta.2020.0450.

[43] Z. Bozóki, J. Sneider, G. Szabó, A. Miklós, M. Serényi, G. Nagy, M. Fehér, Intracavity photoacoustic gas detection with an external cavity diode laser, Appl. Phys. B 63 (4) (1996) 399–401, https://doi.org/10.1007/BF01828745.

[44] I.V. Sherstov, V.A. Vasiliev, A.M. Goncharenko, K.G. Zenov, R.V. Pustovalova, A. I. Karapuzikov, Method for measuring the resonant frequency of photoacoustic detector in the real-time mode, Instrum. Exp. Tech. 59 (5) (2016) 749–753, https://doi.org/10.1134/S0020441216050079.

[45] D.A. Kashtanov, V.A. Vasiliev, A.I. Karapuzikov, I.V. Sherstov, Stabilization of the waveguide CO_2 laser line for a laser photoacoustic SF_6-leak detector, Atmos. Ocean. Opt. 24 (2011) 495–501, https://doi.org/10.1134/S102485601105006X.

[46] I.V. Sherstov, V.A. Vasiliev, K.G. Zenov, R.V. Pustovalova, V.V. Spitcin, S. B. Chernikov, Development and research of a laser photo-acoustic SF_6 gas analyzer, Instrum. Exp. Tech. 60 (3) (2017) 407–413, https://doi.org/10.1134/S0020441217030253.

[47] I.V. Sherstov, V.A. Vasiliev, A.I. Karapuzikov, K.G. Zenov, R.V. Pustovalova, Reducing the energy consumption of a laser photo-acoustic SF_6 gas analyzer, Instrum. Exp. Tech. 61 (4) (2018) 583–589, https://doi.org/10.1134/S0020441218030259.

[48] I. Sherstov, L. Chetvergova, Experimental researches of acoustical modes of various types of resonant photo-acoustic detectors, Opt. Commun. 462 (2020), 124184, https://doi.org/10.1016/j.optcom.2019.125184.

[49] I.V. Sherstov, V.A. Vasiliev, A.I. Karapuzikov, K.G. Zenov, Comparative studies of photo-acoustic gas analyzers based on tunable CO_2 lasers with external and intracavity detector arrangement, Infrared Phys. Technol. 105 (2020), 103170, https://doi.org/10.1016/j.infrared.2019.103170.

[50] I.V. Sherstov, V.A. Vasiliev, Highly sensitive laser photo-acoustic SF_6 gas analyzer with 10 decades dynamic range of concentration measurement, Infrared Phys. Technol. 119 (2021), 103922, https://doi.org/10.1016/j.infrared.2021.103922.

[51] X. Yin, L. Dong, H. Wu, H. Zheng, W. Ma, L. Zhang, W. Yin, S. Jia, F.K. Tittel, Sub-ppb nitrogen dioxide detection with a large linear dynamic range by use of a differential photoacoustic cell and a 3.5W blue multimode diode laser, Sens. Actuators B 247 (2017) 329–335, https://doi.org/10.1016/j.snb.2017.03.058.

[52] X. Yin, L. Dong, H. Wu, H. Zheng, W. Ma, L. Zhang, W. Yin, L. Xiao, S. Jia, F. K. Tittel, Highly sensitive SO_2 photoacoustic sensor for SF_6 decomposition detection using a compact mW-level diode-pumped solid-state laser emitting at 303 nm, Opt. Express 25 (26) (2017) 32581–32590, https://doi.org/10.1364/OE.25.032581.

[53] X. Yin, H. Wu, L. Dong, B. Li, W. Ma, L. Zhang, W. Yin, L. Xiao, S. Jia, F.K. Tittel, Ppb-level SO_2 photoacoustic sensors with a suppressed absorption-desorption effect by using a 7.41 μm external-cavity quantum cascade laser, ACS Sensors 5 (2020) 549–556, https://doi.org/10.1021/acssensors.9b02448.

[54] C.-M. Lee, K.V. Bychkov, A.I. Karapuzikov, I.V. Sherstov, V.A. Vasiliev, V. A. Kapitanov, Y.N. Ponomarev, High-sensitivity laser photoacoustic leak detector, Opt. Eng. 46 (6) (2007), 064302, https://doi.org/10.1117/1.2748042.

[55] A. Miklos, P. Hess, Z. Bozoki, Application of acoustic resonators in photoacoustic trace gas analysis and metrology, Rev. Sci. Instrum. 72 (4) (2001) 1937–1955, https://doi.org/10.1063/1.1353198.

[56] F.G.C. Bijnen, J. Reuss, F.J.M. Harren, Geometrical optimization of a longitudinal resonant photoacoustic cell for sensitive and fast trace gas detection, Rev. Sci. Instrum. 67 (8) (1996) 2914–2923, https://doi.org/10.1063/1.1147072.

[57] F.J.M. Harren, F.G.C. Bijnen, J. Reuss, L.A.C.J. Voesenek, C.W.P.M. Blom, Sensitive intracavity photoacoustic measurements with a CO_2 waveguide laser, Appl. Phys. B 50 (2) (1990) 137–144, https://doi.org/10.1007/BF00331909.

[58] T. Fink, S. Büscher, R. Gäbler, Q. Yu, A. Dax, W. Urban, An improved CO_2 laser intracavity photoacoustic spectrometer for trace gas analysis, Rev. Sci. Instrum. 67 (11) (1996) 4000–4004, https://doi.org/10.1063/1.1147274.

[59] M.M.J.W. Herpen, S. Li, S.E. Bisson, H.S. Lintel, F.J.M. Harren, Tuning and stability of a continuous-wave mid-infrared high-power single resonant optical parametric oscillator, Appl. Phys. B 75 (2) (2002) 329–333, https://doi.org/10.1007/s00340-002-0989-2.

[60] A.A. Kosterev, Y.A. Bakhirkin, F.K. Tittel, S. McWhorter, B. Ashcraft, QEPAS methane sensor performance for humidified gases, Appl. Phys. B 92 (2008) 103–109, https://doi.org/10.1007/s00340-008-3056-9.

[61] V. Spagnolo, P. Patimisco, S. Borri, G. Scamarcio, B.E. Bernacki, J. Kriesel, Part-per-trillion level SF_6 detection using a quartz enhanced photoacoustic spectroscopy-based sensor with single-mode fiber-coupled quantum cascade laser excitation, Opt. Lett. 37 (21) (2012) 4461–4463, https://doi.org/10.1364/OL.37.004461.

[62] A. Sampaolo, P. Patimisco, M. Giglio, L. Chieco, G. Scamarcio, F.K. Tittel, V. Spagnolo, Highly sensitive gas leak detector based on a quartz-enhanced photoacoustic SF_6 sensor, Opt. Express 24 (14) (2016) 15872–15881, https://doi.org/10.1364/OE.24.015872.

[63] H. Wu, L. Dong, X. Yin, A. Sampaolo, P. Patimisco, W. Ma, L. Zhang, W. Yin, L. Xiao, V. Spagnolo, S. Jia, Atmospheric CH_4 measurement near a landfill using an ICL-based QEPAS sensor with V-T relaxation self-calibration, Sens. Actuators B 297 (2019), 126753, https://doi.org/10.1016/j.snb.2019.126753.

[64] G. Menduni, A. Zifarelli, E. Kniazeva, S.D. Russo, A.C. Ranieri, E. Ranieri, P. Patimisco, A. Sampaolo, M. Giglio, F. Manassero, E. Dinuccio, G. Provolo, H. Wu, D. Lei, V. Spagnolo, Measurement of methane, nitrous oxide and ammonia in atmosphere with a compact quartz-enhanced photoacoustic sensor, Sens. Actuators B 375 (7) (2023), 132953, https://doi.org/10.1016/j.snb.2022.132953.

[65] V. Koskinen, J. Fonsen, K. Roth, J. Kauppinen, Cantilever enhanced photoacoustic detection of carbon dioxide using a tunable diode laser source, Appl. Phys. B 86 (2007) 451–454, https://doi.org/10.1007/s00340-006-2560-z.

[66] T. Tomberg, M. Vainio, T. Hieta, L. Halonen, Sub-parts-per-trillion level sensitivity in trace gas detection by cantilever-enhanced photo-acoustic spectroscopy, Sci. Rep. 8 (1) (2018) 1848, https://doi.org/10.1038/s41598-018-20087-9.

[67] P. Varanasi, Z. Li, V. Nemtchinov, A. Cherukuri, Spectral absorption-coefficient data on HCFC-22 and SF_6 for remote-sensing applications, J. Quant. Spectrosc. Radiat. Transf. 52 (3–4) (1994) 323–332, https://doi.org/10.1016/0022-4073(94)90162-7.

[68] A. Kachanov, S. Koulikov, F.K. Tittel, Cavity-enhanced optical feedback-assisted photo-acoustic spectroscopy with a 10.4 μm external cavity quantum cascade laser, Appl. Phys. B 110 (2013) 47–56, https://doi.org/10.1007/s00340-012-5250-z.

[69] P. Patimisco, S. Borri, I. Galli, D. Mazzotti, G. Giusfredi, N. Akikusa, M. Yamanishi, G. Scamarcio, P.D. Natale, V. Spagnolo, High finesse optical cavity coupled with a quartz-enhanced photoacoustic spectroscopic sensor, Analyst 140 (2015) 736–743, https://doi.org/10.1039/C4AN01158A.

[70] T. Tomberg, T. Hieta, M. Vainio, L. Halonen, Cavity-enhanced cantilever-enhanced photo-acoustic spectroscopy, Analyst 144 (2019) 2291–2296, https://doi.org/10.1039/C9AN00058E.

[71] M. Kaliszewski, M. Włodarski, J. Młyńczak, B. Jankiewicz, L. Auer, B. Bartosewicz, M. Liszewska, B. Budner, M. Szala, B. Schneider, G. Povoden, K. Kopczyński, The Multi-Gas Sensor for Remote UAV and UGV Missions - Development and Tests, Sensors 21 (22) (2021) 7608, https://doi.org/10.3390/s21227608.

[72] A. Szczurek, D. Gonstal, M. Maciejewska, The Gas Sensing Drone with the Lowered and Lifted Measurement Platform, Sensors 23 (3) (2023) 1253, https://doi.org/10.3390/s23031253.

[73] Y. Zheng, S. Yang, X. Liu, J. Wang, T. Norton, J. Chen, Y. Tan, The computational fluid dynamic modeling of downwash flow field for a six-rotor UAV, Front. Agric. Sci. Eng. 5 (2) (2018) 159–167, https://doi.org/10.15302/J-FASE-2018216.

[74] H.J. Jumaah, B. Kalantar, A.A. Halin, S. Mansor, N. Ueda, S.J. Jumaah, Development of UAV-Based PM2.5 Monitoring System, Drones 5 (3) (2021), https://doi.org/10.3390/drones5030060.